In situ coastal observations of wave homogeneity and coherence

Konstantinos Christakos [a,b,*], Zhen Gao [a], Birgitte R. Furevik [b,c], Jan-Victor Björkqvist [b,d,e], Ole Johan Aarnes [b]

[a] Department of Marine Technology, Norwegian University of Science and Technology (NTNU), Trondheim, 7491, Norway
[b] Norwegian Meteorological Institute, Allégaten 70, 5007 Bergen, Norway
[c] Geophysical Institute, University of Bergen, Allégaten 70, 5007 Bergen, Norway
[d] Finnish Meteorological Institute, Erik Palménin aukio 1, 00560 Helsinki, Finland
[e] Tallinn University of Technology, Department of Marine Systems, Akadeemia tee 15a, 12618 Tallinn, Estonia

ARTICLE INFO

ABSTRACT

A better understanding of wave homogeneity, i.e. the spatial variations of the wave characteristics, and wave coherence in coastal areas and fjords is essential for the design and analysis of sea-crossing infrastructures, such as floating bridge concepts. The wave conditions in fjords that are exposed to the open sea are complex and often characterized by a mixed swell–wind sea state. This study investigates the spatial coherence and homogeneity of ocean waves using two years of unique buoy observations from Sulafjorden – a fjord partly exposed to the open sea. We analyze both long term statistics and four selected cases with different sea states. The most exposed locations are dominated by long waves (swell), while the energy of the wind sea is comparable to the swell energy in the more sheltered locations. Despite the study area being relatively small (ca. 2 km ×1 km), the differences in wave conditions are significant because the complex fjord geometry blocks the incoming offshore waves, and changes in fetch and wind conditions affects the local wave growth. For swell waves we measured an along-crest spatial coherence (ca. 0.6) over a 1–2 km distance. The coherence between consecutive crests for swell was weaker (up to 0.3–0.4) for distances between 0.6 km and 1.3 km (up to about 5 wavelengths). Wind sea (both along crest and between crests) showed no coherence over these distances.

1. Introduction

Information on environmental conditions, such as wind, waves, and currents, is vital for designing marine structures, where it is needed for response, load and fatigue calculations. The structures may be floating bridges, submerged tunnels, wind turbines, solar panels, wave energy converters, and fish farms in nearshore locations. Large floating structures for coastal infrastructure, aquaculture and renewable energy applications cover large surface areas, and the inhomogeneity of ocean waves should therefore be taken into consideration (Aksnes et al., 2022).

In complex coastal areas, such as the Norwegian coast with its thousands of islands, islets and narrow fjords, accurate knowledge of environmental conditions is a crucial part of the structural design. The wave conditions along the west coast of Norway are characterized by mixed swell–wind sea conditions. Swell waves are long-crested surface waves whose phase velocity exceeds the local wind speed or propagates across the wind direction. The most energetic swell waves along the coast are observed in the Norwegian Sea due to its direct exposure to

the Atlantic Ocean (e.g., Semedo et al., 2014; Christakos et al., 2020b). Short-crested, irregular, waves under the influence of the local wind are known as wind sea. Extra-tropical cyclones and coastal orographic phenomena causes the wind sea to vary significantly more in both time and space compared to the more regular swell waves.

The fjord axis (line parallel to shore) steers the dominant wave direction, and the wave conditions inside fjords therefore differ significantly from a typical coastal climate. Swell propagation depends on the exposure to the open sea, while the local wind sea is strongly affected by the orography and fjord geometry. In fjords exposed to the open sea, the offshore waves (e.g., swell or old wind sea) dominate the wave climate. The narrow fjord geometry permits penetration of a certain swell direction, thus not allowing the coexistence of multiple swell systems in the fjords. At the same time, the local wind sea can also be relatively strong depending on the fjord geometry, the exposure to the open sea and the weather conditions. The local wind dominates the wave climate in fjords sheltered from the open sea where swell is nearly absent.
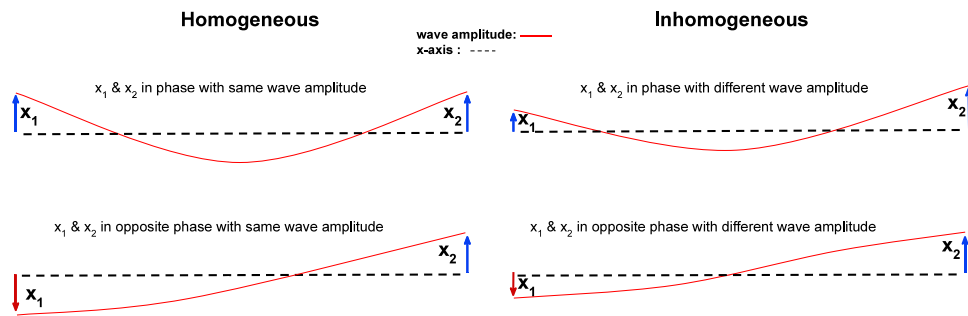
Fig. 1. Schematic illustration of coherent—homogeneous/inhomogeneous wave conditions between two sea points (x_1 and x_2) along x-axis e.g., the axis of a marine structure. The red curve represents the wave amplitude. The arrows show the vertical displacement at x_1 and x_2.

Based on the National Transport Plan 2022–2033 (The Norwegian Ministry of Transport, 2020), Norway aims to develop a modern transport system for faster and safer travel and transport of goods. One of the important components of this plan is the Coastal Highway Route E39 project led by the Norwegian Public Roads Administration (NPRA). The project's goal is to design and construct bridges and tunnels that are replacing existing ferry connections along the route between Kristiansand and Trondheim (Dunham, 2016). In this regard, met-ocean observations and simulations are essential for load and response calculations. Penetration of low-frequency waves, i.e. swell in fjords, can induce large vertical oscillations in such structures (Aalberg, 2017). In addition, the wave field inhomogeneity in a fjord can be associated with a possible response and fatigue damage of a floating bridge (Dai et al., 2021b). Recent studies have shown that the wave conditions in Norwegian fjords can be inhomogeneous (Cheng et al., 2021; Dai et al., 2021a). Nonetheless, phase-averaged wave simulations have revealed that the change in wave conditions along a proposed crossing in Sulafjorden was gradual (Dai et al., 2021a).

Most marine structures are relatively short in length compared to the wavelength of dominant waves. Therefore, information about the wave conditions at one location is sufficient for designing such structures. However, novel offshore and coastal structures, like offshore wind farms, floating bridges, fish farms and solar panels, may cover a large area (in the order of 1–5 km^2), where the wave conditions may vary spatially.

During the design process of marine structures, it is commonly assumed that the wave conditions are homogeneous and coherent. A wave field is considered homogeneous if the average properties at each location are identical. If the surface elevations for any pair of locations are coherent, the wave field is considered coherent. Even if the wave field is coherent, changes in phase and homogeneity between two points located along the axis of a marine structure can cause different responses as illustrated in Fig. 1.

The assumptions of homogeneity and coherence seem reasonable for open sea applications, but they might be invalid in complex coastal areas like a fjord system. The fjord topography can lead to spatial variation in both wave density spectra and coherence. The coherence of ocean waves has not been studied to the same degree as wind coherence, where different models have been established, such as the Mann uniform shear model (Mann, 1994) and the exponential coherence model (the Kaimal model, International Eletrotechnical Commision (2005)).

The interference of coherent waves nearshore can affect wave processes and create spatial variations (inhomogeneity) in wave characteristics. According to Salatin et al. (2021), coherent waves can result in stationary interference in the longshore variability of the nearshore wave height and mean sea level. Smit et al. (2015) simulated coherent effects near Scripps Canyon due to refractive focusing of swell waves that leads to variations in the wave field.

Our overall objectives are to find which wave conditions are associated with different coherence levels and how the coastal geometry and
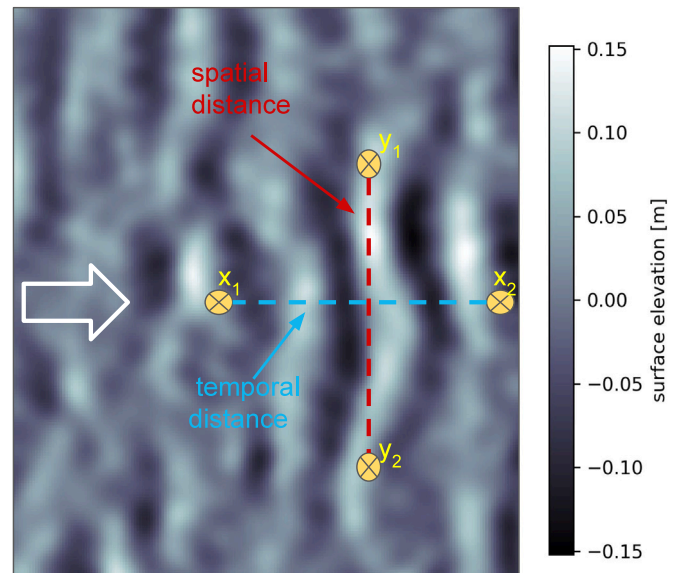

Fig. 2. Surface elevation of irregular waves and pairs of points located across and along the propagation direction (white arrow). The coherence measured at different pairs can be formed in the following ways by measuring: the same wave as it spans in space (y_1&y_2; points across the propagation direction), the same wave with a time lag (x_1&x_2; points along the propagation direction), or a combination of the two (e.g., x_1&y_1). Simulation of surface elevation was performed using the non-hydrostatic numerical model SWASH (Zijlema et al., 2011).

the local wind affect the wave homogeneity and coherence. This will be achieved using a unique data set consisting of wave buoy observations from devices moored near each other. The data was obtained in the Sulafjorden, a fjord partly exposed to the Norwegian Sea. To our knowledge, this is the first study that investigates both homogeneity and coherence using long-term in situ observations.

The paper is organized as follows: Section 2 describes the data and methods employed, followed by Section 3, which presents the overall results and selected case studies. In Section 4, we discuss the results, and in Section 5, we finish by summarizing and concluding our findings.

2. Data and methods

2.1. Homogeneity

The word homogeneous comes from the Ancient Greek word ὁμογενής (homogenes). It contains the words ὁμός (homos, "same") + γένος (genos, "kind") and it means "the same kind". In random processes such as the sea surface elevation, the data is considered
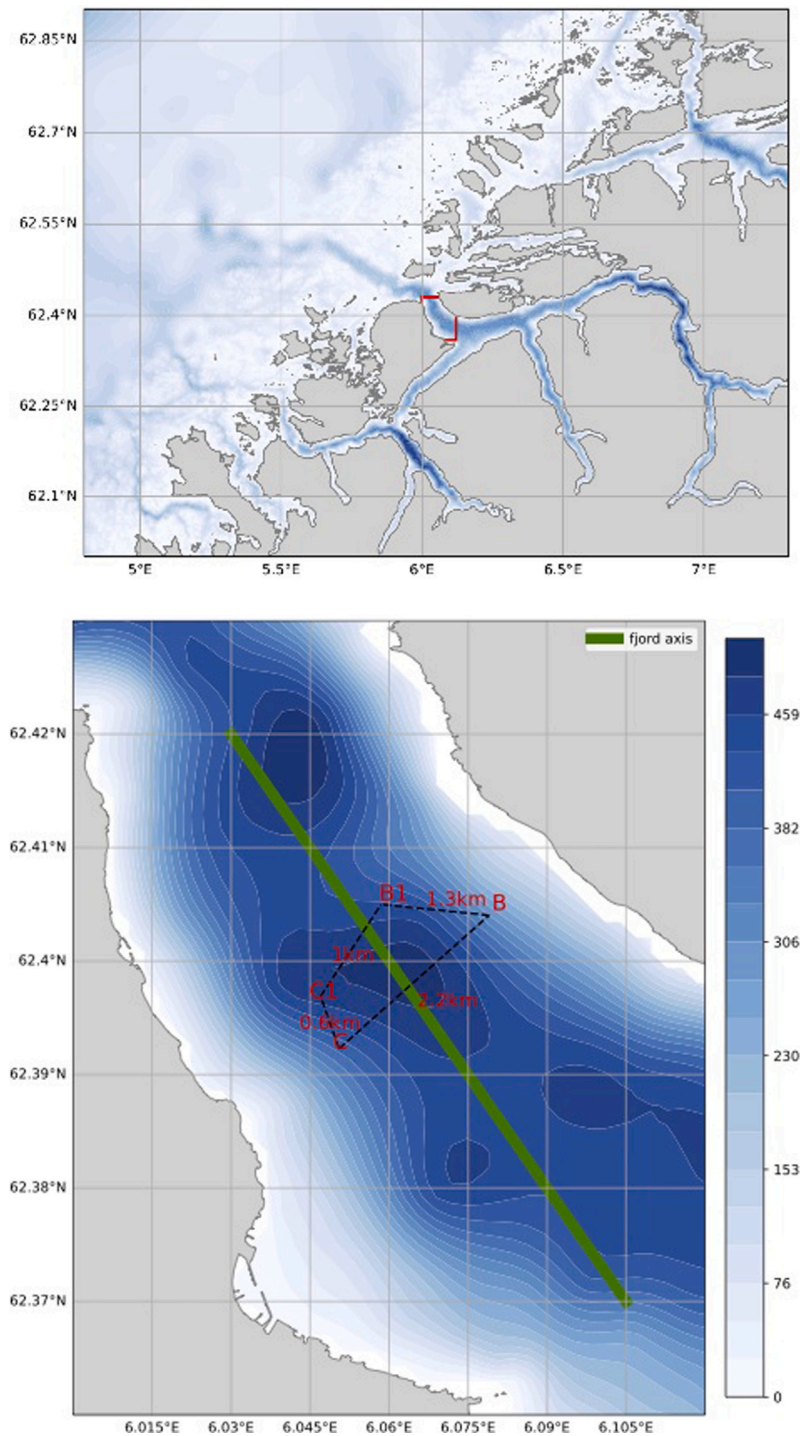
Fig. 3. Location of Sulafjorden (red) in the west coast of Norway (top). Position of buoys B, B1, C and C1 with the corresponding average distances in km (bottom). The color bar shows the depth in meters, derived by Sjødivisjon (2015).

homogeneous if its average characteristics do not vary in space, similar to being stationary in time (Bendat and Piersol, 2010). Therefore, we consider an ocean wave field to be homogeneous if the power spectral density (S) for each location (e.g., x_1, x_2) are identical, i.e. for all frequencies (f) and wave directions (θ)

$$\Delta S_{x_1 x_2}(f, \theta) = S_{x_1}(f, \theta) - S_{x_2}(f, \theta) \approx 0 \text{ (for directional data), or} \quad (1)$$

$$\Delta S_{x_1 x_2}(f) = S_{x_1}(f) - S_{x_2}(f) \approx 0 \text{ (for omnidirectional data),} \quad (2)$$

where $S_{x_1}(f, \theta)$ and $S_{x_2}(f, \theta)$ are the directional power spectral density at x_1 and x_2 locations, respectively. The corresponding omnidirectional frequency power spectral density functions are $S_{x_1}(f) = \int_0^{2\pi} S_{x_1}(f, \theta) \, d\theta$ and $S_{x_2}(f) = \int_0^{2\pi} S_{x_2}(f, \theta) \, d\theta$. These conditions result in the same sea state parameters, such as significant wave height (H_s) and peak wave period (T_p). Conversely, an inhomogeneous wave field is mathematically described with $|\Delta S_{x_1 x_2}(f, \theta)| \gg 0$ (directional) or $|\Delta S_{x_1 x_2}(f)| \gg 0$ (omnidirectional), keeping in mind that measured wave spectra have
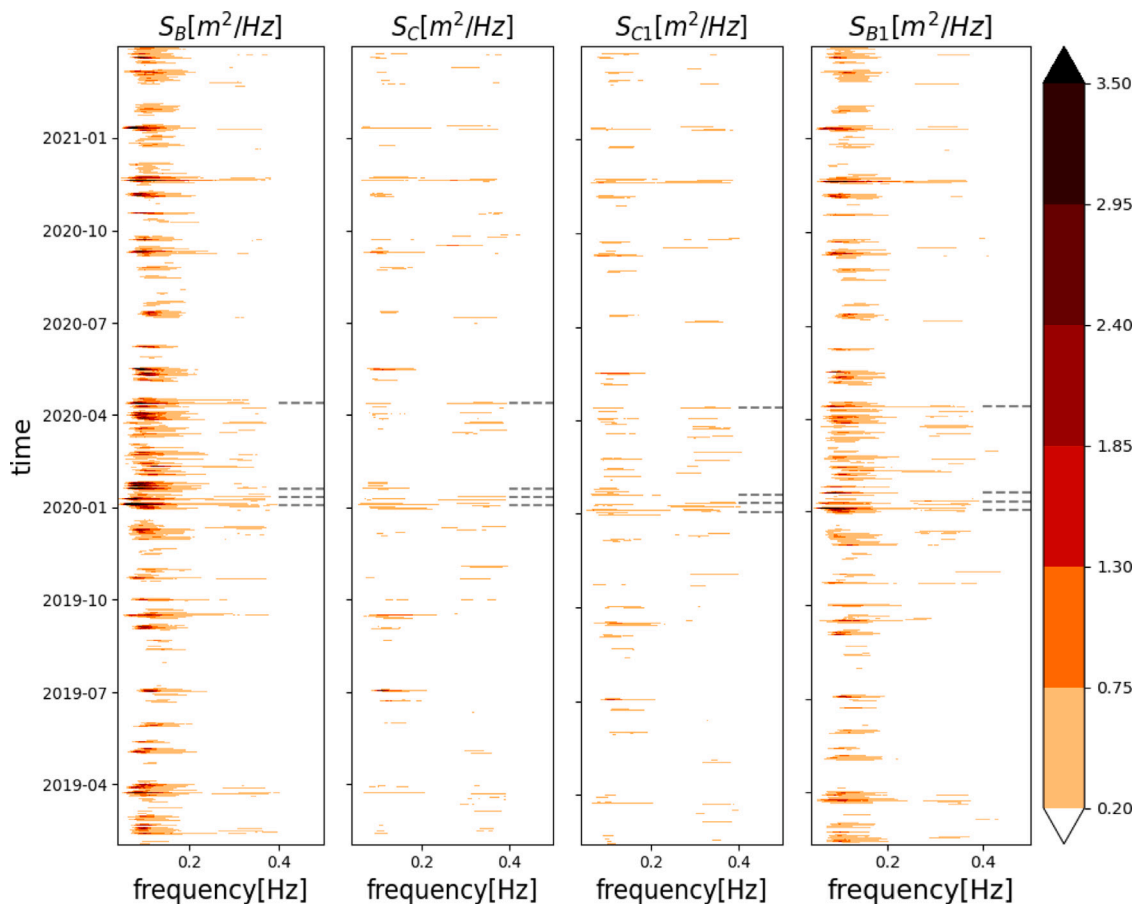
Fig. 4. Power spectral density as a function of time and frequency for the period February 1, 2019 to March 31, 2021. The case studies (Section 3.3) are indicated with the gray dashed lines.

random sampling variability (Donelan and Pierson, 1983; Forristall et al., 1996).

2.2. Coherence

The word coherence comes from the Latin *cohaerere* consisting of *co-* ("together") and *haerere* ("to stick, adhere"). In physics, coherent waves are pairs of waves having the same frequency and waveform with a constant phase difference. For surface ocean waves (numerous frequencies), the coherence indicates how well the surface elevation $\eta(t)$ between two points are related to each other at different frequencies. If the two wave signals are coherent, they can be related by a linear transfer function, $H(f)$, in frequency space ($S_{x_1}(f) = |H(f)|^2 \cdot S_{x_2}(f)$). To quantify the coherence, we use the magnitude squared coherence function $C_{x_1 x_2}$ between the surface elevation at locations x_1 and x_2 as given by (e.g., Mandel and Wolf, 1995; Stoica and Moses, 2005):

$$C_{x_1 x_2}(f) = \frac{|S_{x_1 x_2}(f)|^2}{S_{x_1}(f) S_{x_2}(f)}, \tag{3}$$

where $S_{x_1 x_2}$ is the cross power spectral density of the two signals. The coherence varies from 0 to 1. If $C_{x_1 x_2}$ is one, the two signals are entirely related, while $C_{x_1 x_2} \approx 0$ indicates nearly no relation, i.e., having a random or varying phase relationship. In practice, $C_{x_1 x_2}$ greater than roughly 0.5 show considerable coherence ($C_{x_1 x_2}^{1/2} \approx 0.7$).

Coherence varies with the distance between the two positions. In the present study, relative changes in buoys' distances are insignificant (due to distances $\geq$ 600 m and anchoring). Coherence is also related to the wave propagation direction relative to the buoy positioning (along or perpendicular to wave direction). This relationship is discussed in more detail in the following sections.

In practice, the coherence measured between two sea points can be formed in different ways, as illustrated in Fig. 2, by measuring (i) the same wave as it spans in space (pairs located across the propagation direction), (ii) the same wave with a time lag (pairs located along the propagation direction), or (iii) a combination of the two. Therefore, the coherence can be considered both as a measure of crest wavelength and an indication of how well a wave preserves its phase information as it propagates.

Figs. A.12, A.13 and A.14 in Appendix illustrate artificial surface elevations, the corresponding spectral densities and coherence for incoherent-homogeneous, coherent-inhomogeneous and coherent-homogeneous waves conditions.

2.3. In situ observations

The fjord studied is Sulafjord, located on the west coast of Norway within the Møre and Romsdal county, is an area with complex coastal wind conditions (Christakos et al., 2013, 2014). The location of the fjord is shown in Fig. 3. The fjord is about 10 km long and has an average width of about 5 km. Four Wavescan buoys (FUGRO, 2012) B, C, C1 and B1 are deployed in the center of Sulafjorden (area: ca 2 km x 1 km). C & C1 buoys are located at 0.6 km, B & C at 2.2 km, B & B1 at 1.3 km, and B1 & C1 at 1 km apart. The observations used in this study cover two years from February 1, 2019, to March 31, 2021, where all four buoys were operating (Note: no available raw wave data from February 2020 at location C during the study). In our analysis, only cases with total H_s greater than 0.2 m are considered for all locations.
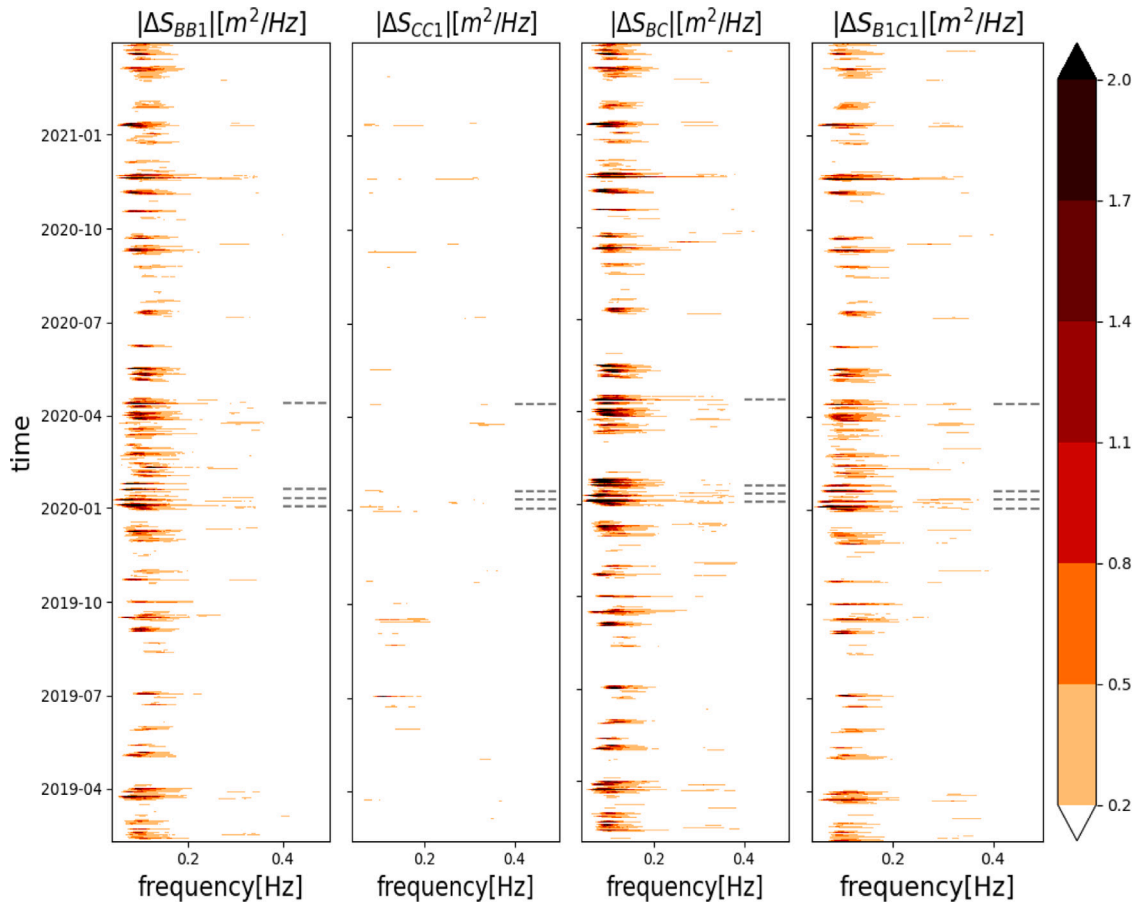
Fig. 5. Absolute difference of frequency spectrum $|\Delta S(f)|$ over time between different pairs for the period February 1, 2019 to March 31, 2021. The case studies (Section 3.3) are indicated with the gray dashed lines.

2.3.1. Directional spectrum

The heave, compass, pitch and roll buoy data (in 17 min samples) is available via the Thredds Service at the Norwegian Meteorological Institute (Furevik et al., 2020). The computation of the frequency spectrum, $S(f)$, is based on the Welch method (Welch, 1967). The directional spreading, $D(f,\theta)$, is estimated based on the Maximum Entropy Method (Radoski et al., 1975) using the first four Fourier coefficients, which are derived from the auto- and cross-spectrum of heave, North–South and West–East slopes (e.g., Longuet-Higgins, 1963; Ananth et al., 1993; Brissette and Tsanis, 1994; Steele et al., 1998; Lygre and Krogstad, 1986). Finally, the directional power spectral density at a location x is defined as:

$$S_x(f,\theta) = S_x(f)D_x(f,\theta) \tag{4}$$

The source code for the computation of the directional spectrum is available at Christakos (2021).

2.4. Identification of swell and wind sea

The identification of swell and wind sea is based on the formulation by Komen et al. (1984):

$$A = \beta \frac{U_{10}\cos(\theta - \theta_w)}{c_{ph}} \tag{5}$$

where $\beta(=1.3)$ is a calibration factor (≤ 1.3 is recommended for identification of pure wind sea conditions according to e.g., Hasselmann et al. (1996)), U_{10} is the wind speed at height 10 m, c_{ph} is phase speed, θ is the wave direction, and θ_w is the wind direction. The condition $A > 1$ represent swell components while $A \leq 1$ indicates wind-sea.

We apply the logarithmic wind profile to adjust the observed wind speed from 4.1 m (U_w) to 10 m (U_{10}) using a roughness length of 0.0002 m (e.g., Christakos et al., 2020a).

3. Results

3.1. Homogeneity: Long-term statistics

The wave climate in Sulafjorden is mainly dominated by waves coming from the open ocean (offshore waves). Within the study area, the locations most exposed to the open sea (B & B1) are dominated by long waves (<0.15 Hz), as presented in Fig. 4. In the most sheltered locations to offshore waves (C & C1), we observe that shorter waves, associated with wind sea, have a power density comparable to longer waves (i.e. lower frequency waves such as swell).

The absolute difference of frequency spectrum $|\Delta S(f)|$ over time between the pairs B & B1, C & C1, B & C, and B1 & C1, illustrated in Fig. 5, provides an indication of homogeneity over time. Pairs in the closest distance (C & C1), show nearly homogeneous conditions (low $|\Delta S(f)|$) for most of the time. On the other hand, the pair B & C, located across the fjord axis, shows inhomogeneous conditions (high $|\Delta S(f)|$) for most of the time in low frequencies (<0.15 Hz).

Fig. 6 shows the degree of inhomogeneity of the wave field between two locations, as measured by the difference in the directional wave spectra $\overline{|\Delta S(f,\theta)|}$. The strongest inhomogeneity (high $\overline{|\Delta S(f,\theta)|}$) is observed at northwest directions representing a penetration of long waves. In contrast, lower $\overline{|\Delta S(f,\theta)|}$ values are detected in south/southeast directions associated with shorter waves (locally generated wind sea). The magnitude of $\overline{|\Delta S(f,\theta)|}$ for the wind sea part of the spectrum is similar between the locations. However, the magnitude
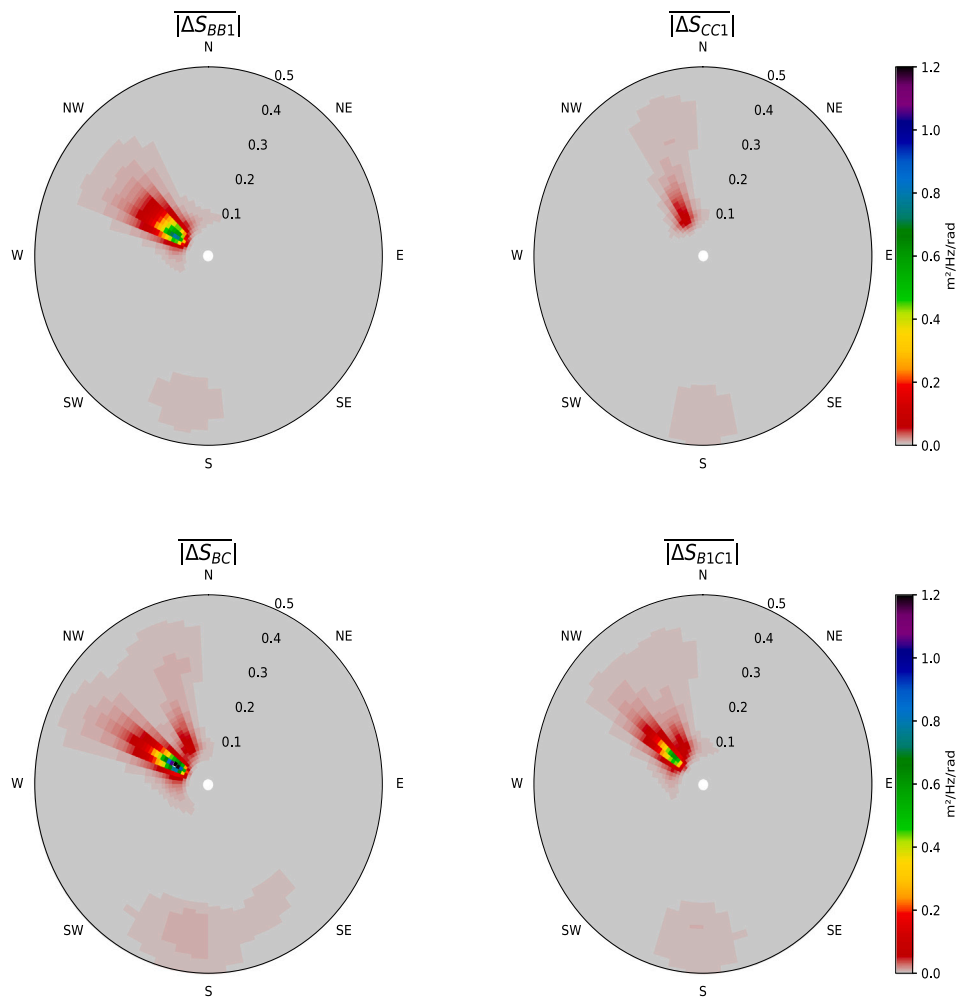
Fig. 6. Average difference of directional spectrum ($\overline{|\Delta S(f,\theta)|}$) between two locations for the period February 1, 2019 to March 31, 2021.

of incoming long waves shows significant differences, especially in pair B & C.

For swell, as seen in Fig. 7 (top), the lowest wave height ratio ($\frac{\bar{y}}{\bar{x}}$) is observed between buoys located across (perpendicular to) the fjord axis (0.45 and 0.58 at C & B and C1 & B1, respectively). We also observe the lowest correlation coefficient (r^2), 0.40 and 0.54 at C & B and C1 & B1, respectively. Pair of locations along to the fjord axis show a much higher H_{m0} ratio, 0.8 at B1 & B and 1.04 at C1 & C, while the correlation coefficients at these pairs are 0.78 and 0.92.

Compared to swell, wind sea conditions (Fig. 7, bottom) show higher correlation coefficients and more similar magnitudes of H_{m0} between neighboring buoy location. For locations across the fjord axis, B & C and B1 & C1, the ratio of H_{m0} is about 0.7 and the correlation coefficient 0.48 and 0.70, respectively. Pair of locations along the fjord axis shows a ratio close to 0.9–1, while the correlation coefficients at these pairs are about 0.9.

3.2. Coherence: Long-term statistics

For long waves the buoy pairs located across the fjord axis (B1 & C1 and C & B) measure coherence along crest, while the pairs along the fjord axis (B & B1 and C & C1) measure coherence between crests. The mean and 95th percentile (sorted over time at each frequency bin) of power spectral density and coherence is illustrated in Fig. 8. The highest coherence for the mean (0.25) and 95th percentile (0.6) is observed for locations across the fjord axis (B & C and B1 & C1). The maximum coherence at the 95th percentile has a wave frequency of

about 0.08 Hz (wavelength $\approx$ 244 m) and a wave height of ca. 0.2 m. For very low frequencies (<0.05 Hz; wavelength > 625 m), the wave energy is close to zero. For high frequencies (>0.15 Hz; wavelength < 70 m), the coherence rapidly decreases to nearly zero. The frequency of the dominant waves is 0.1 Hz (wavelength $\approx$ 160 m), slightly higher than the frequency of the highest coherence. The coherence of these waves is about 0.4 for the 95th percentile and below 0.2 for the mean.

For the pairs along the fjord axis (B & B1 and C & C1), the coherence is low, below 0.12 for the mean and 0.35 for the 95th percentile.

Fig. 9 illustrates the wave coherence as a function of time and frequency for the period February 1, 2019 to March 31, 2021. For pairs located along to the fjord axis (B & B1) the coherence is high only for very low frequencies. In May 2020, we observed some events with high coherence ($C > 0.7$). These episodic events are associated with very low frequencies and low wave heights (illustrated by Fig. A.15). For C & C1, due to their proximity (ca. 600 m), we also observe elevated coherence values in high frequencies (≥ 0.2 Hz). A strong wave coherence in low frequencies (<0.1 Hz; wavelength>160 m) is detected for locations across the fjord axis (B & C and B1 & C1). In these cases, the pairs of buoys experience the same wave as it spans in space (e.g., located along the same crest/trough). This means that length of the crest should be about the buoys' distance (1–2 km), i.e., for wavelengths $\geq$ 160 m, the length of the crest should be $\geq$1 km.

3.3. Case studies

In this section we present four selected cases (Table 1) with different sea states to investigate the wave homogeneity and coherence in the
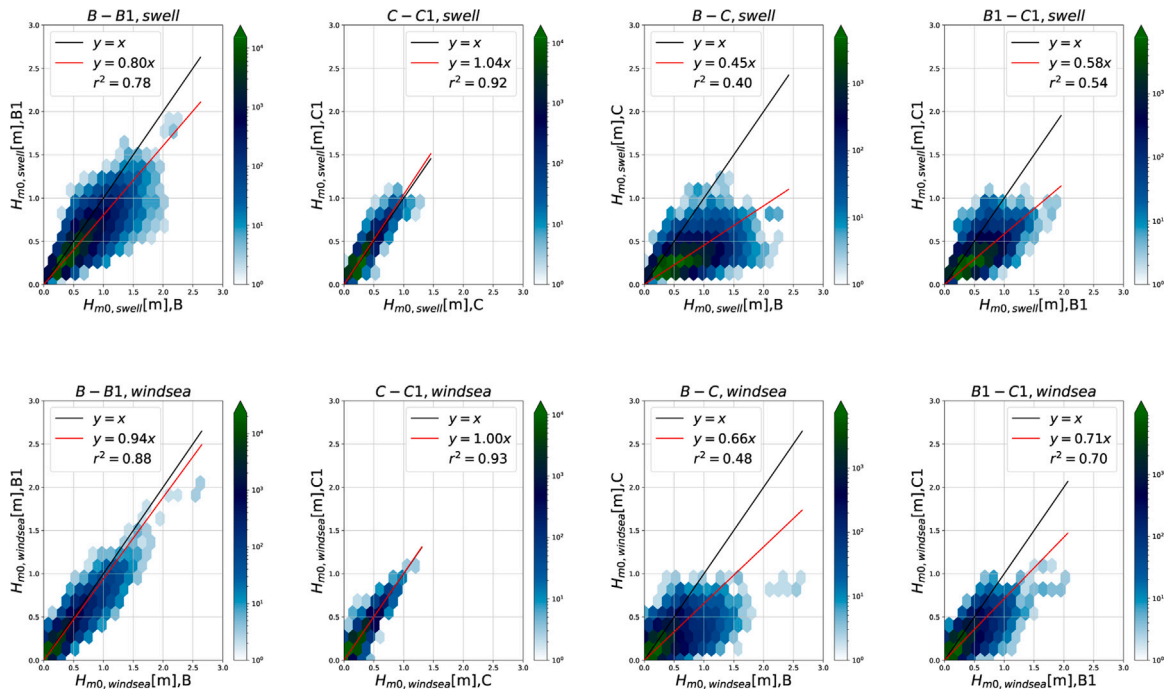
Fig. 7. Scatter plots of significant wave height (H_{m0}) for swell (top) and wind sea (bottom) between two neighbor locations, with the corresponding $y = \frac{\bar{y}}{\bar{x}}x$ (red line), $y = x$ (black line) and correlation coefficient (r^2), for period February 1, 2019 to March 31, 2021. The color indicates the number of data points.
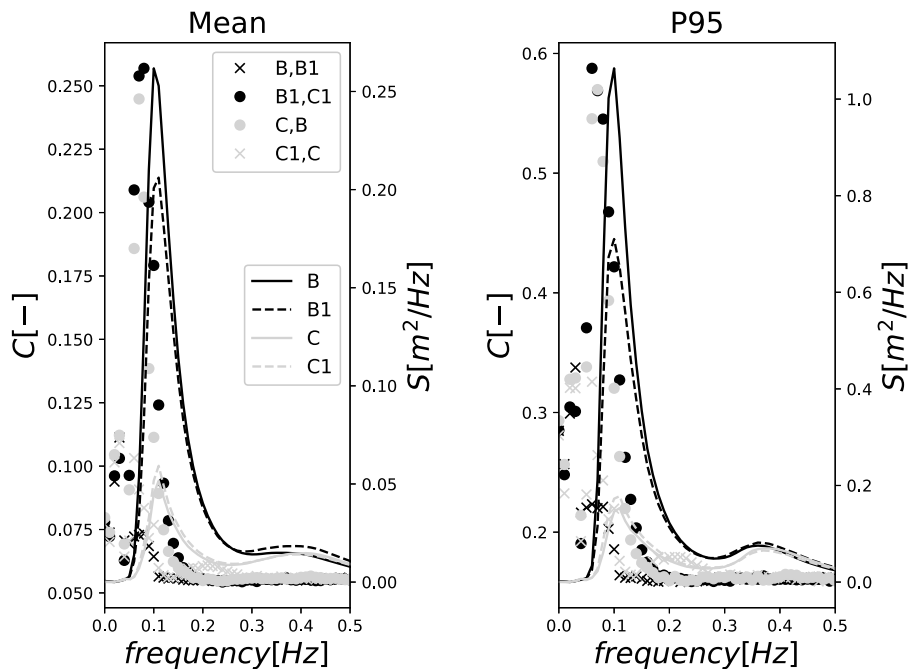

Fig. 8. Mean and 95th percentile of coherence and density spectrum for the buoy locations B, B1, C and C1 for the period February 1, 2019 to March 31, 2021.

fjord. Case I represents an energetic swell propagation within the fjord, case II represents a strong wind sea, while cases III–IV represent different mixed sea states. Fig. 10 shows the directional spectra of the four buoys together with integrated wave parameters, wind and current speed during the different cases. Fig. 11 presents the frequency spectra and the coherence between different pairs of buoys.

3.3.1. Case I : Swell

Case I illustrates high coherence for pairs located both along and across the fjord axis during swell conditions. On January 19, 2020,

Table 1
Case studies.

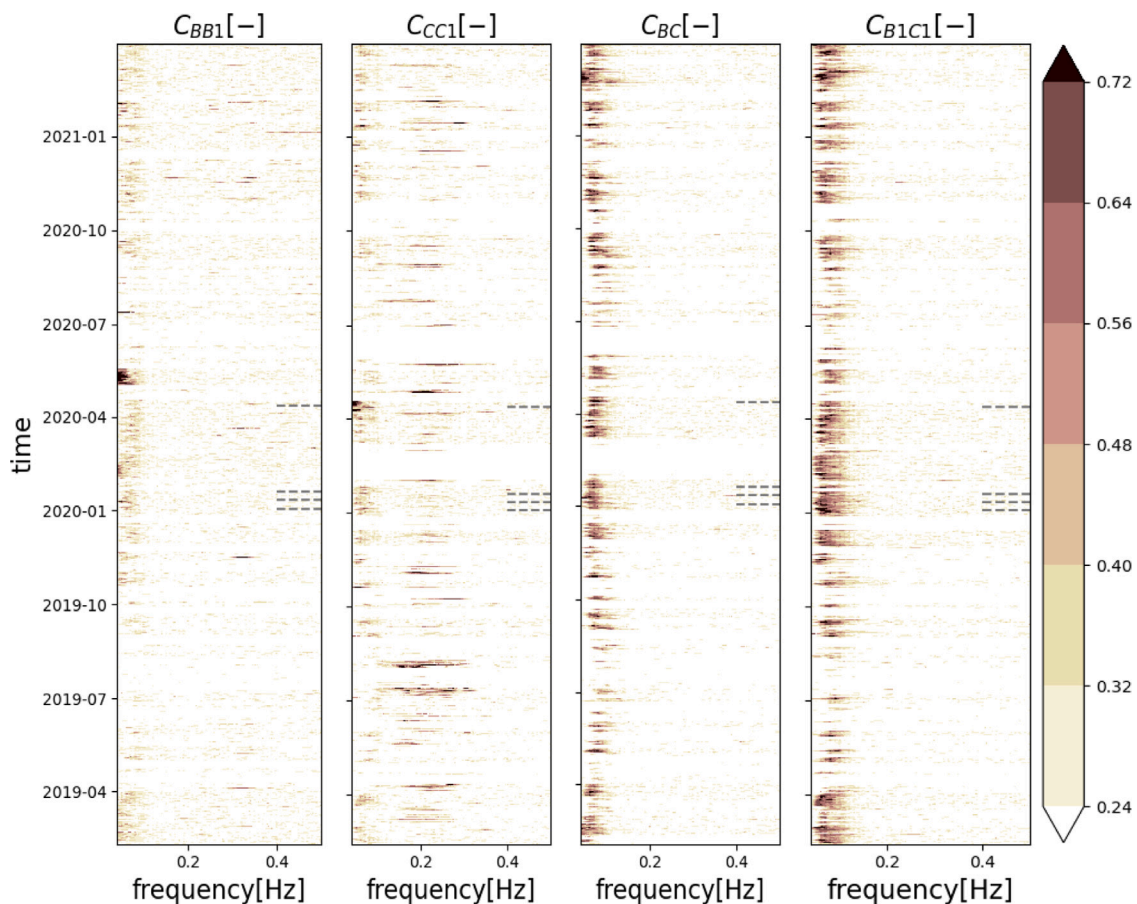| Case	Conditions	Period
I	Swell	2020-01-19T05:00-06:00
II	Wind Sea	2020-01-11T01:00-02:00
III	Swell and Wind Sea (aligned)	2020-04-12T17:30-18:30
IV	Swell and Wind Sea (opposing)	2020-01-02T09:00-10:00

Fig. 9. Coherence as a function of time and frequency between different pairs for the period February 1, 2019 to March 31, 2021. The case studies (Section 3.3) are indicated with the gray dashed lines.

swell waves (T_p of 11–12 s) penetrated Sulafjorden from the open sea (northwest) with winds $\leq$ 7.5 m/s and surface currents $\leq$ 0.4 m/s (Fig. 10). The pair C & C1 shows significantly lower values (80%–95% decrease) in the spectral density peak compared to pair B & B1 (Fig. 11). We observe a high wave coherence for B & C (0.5) and B1 & C1 (0.6) at low frequencies (<0.1 Hz). For pairs along the fjord axis (B & B1 and C & C1), the spectral density peak is reduced by about 40%–45% (from B to B1 and from C1 to C). The highest coherence is detected at low frequencies (ca. 0.05 Hz or wavelength $\approx$ 0.6 km) close to 0.3 for B & B1 (distance: 1.1 km) and 0.5 for C & C1 (distance: 0.6 km).

3.3.2. Case II: Wind sea

Case II describes nearly homogeneous but incoherent conditions during a strong wind sea event in the fjord. On January 11, 2020, strong winds (up to 17 m/s) from the south generated local wind sea (T_p at 3 s) in Sulafjorden with a surface current of 0.5–0.6 m/s from the same direction (Fig. 10). A relative weak swell (with ca. 10 times lower energy than the wind sea at B1) from the open ocean is also present. During these wind sea dominated conditions, the significant wave height and the peak frequency are ca. 0.8–1.0 m and 0.28–0.34 Hz at all locations (Fig. 11). We observe about 13% and 40% lower peak values of the density spectra (S_{max}) from locations B to C and from B1 to C1, respectively. On the other hand, for pairs of buoys located along the fjord axis (B & B1 and C & C1), the spectral shape is nearly identical with minor differences at S_{max}. We observe coherence below 0.2 for frequencies greater than 0.1 Hz (wavelength <150 m) at all different pairs (along and across to the fjord axis) for this short-crested sea.

3.3.3. Case III: Swell and wind sea in the same direction (aligned)

Case III presents strong coherent conditions for low frequencies during aligned swell-wind sea conditions. On April 12, 2020, strong winds (up to 15 m/s) from the northwest generated local wind sea in Sulafjorden, building on energetic swell waves from the same direction (Fig. 10). A surface current of 0.4–0.6 m/s from the northwest is also observed. During these swell-dominated conditions, the B and B1 locations have a peak frequency of about 0.1 Hz, while the wind sea is dominant in the C and C1 areas, where the peak frequencies are about 0.35 Hz. The significant wave height varies between 0.9 m (C,C1) and 1.4–1.5 m (B,B1). We observed a reduction in the peak of density spectra (S_{max}) along the fjord of 29% (B to B1) and 14% (C to C1). The coherence is greater than 0.5 at low-frequency waves in locations across the fjord axis and below 0.2 for frequencies greater than 0.1 Hz (for all different pairs).

3.3.4. Case IV: Swell and wind sea in opposing directions

Case IV illustrates incoherent conditions during opposing swell–wind sea conditions. On January 02, 2020, winds (up to 14 m/s) from south generated local wind sea (T_p of 3 s at C and C1), while swell propagates from almost opposite directions (Fig. 10). The surface current is nearly absent (0.1 m/s). The more exposed north-easterly buoys (B and B1) measured a swell dominated wave field ($f_p \approx$ 0.1 Hz), while the wind sea ($f_p \approx$ 0.4 Hz) dominated at the more sheltered south-westerly pair (C & C1), as illustrated in Fig. 11. The significant wave height varies between 0.6 m (C & C1) and 0.8–1.0 m (B & B1). We observe a reduction of 20% and 13% in the peak of density spectra (S_{max}) from locations B to B1 and C to C1, respectively (Fig. 11). The highest coherence is ca. 0.3 at 0.1 Hz in pair B1 & C1 and below 0.2 for frequencies greater than 0.1 Hz for all different pairs. The wind sea at locations B & B1 and C & C1 show minor difference in spectral shape.
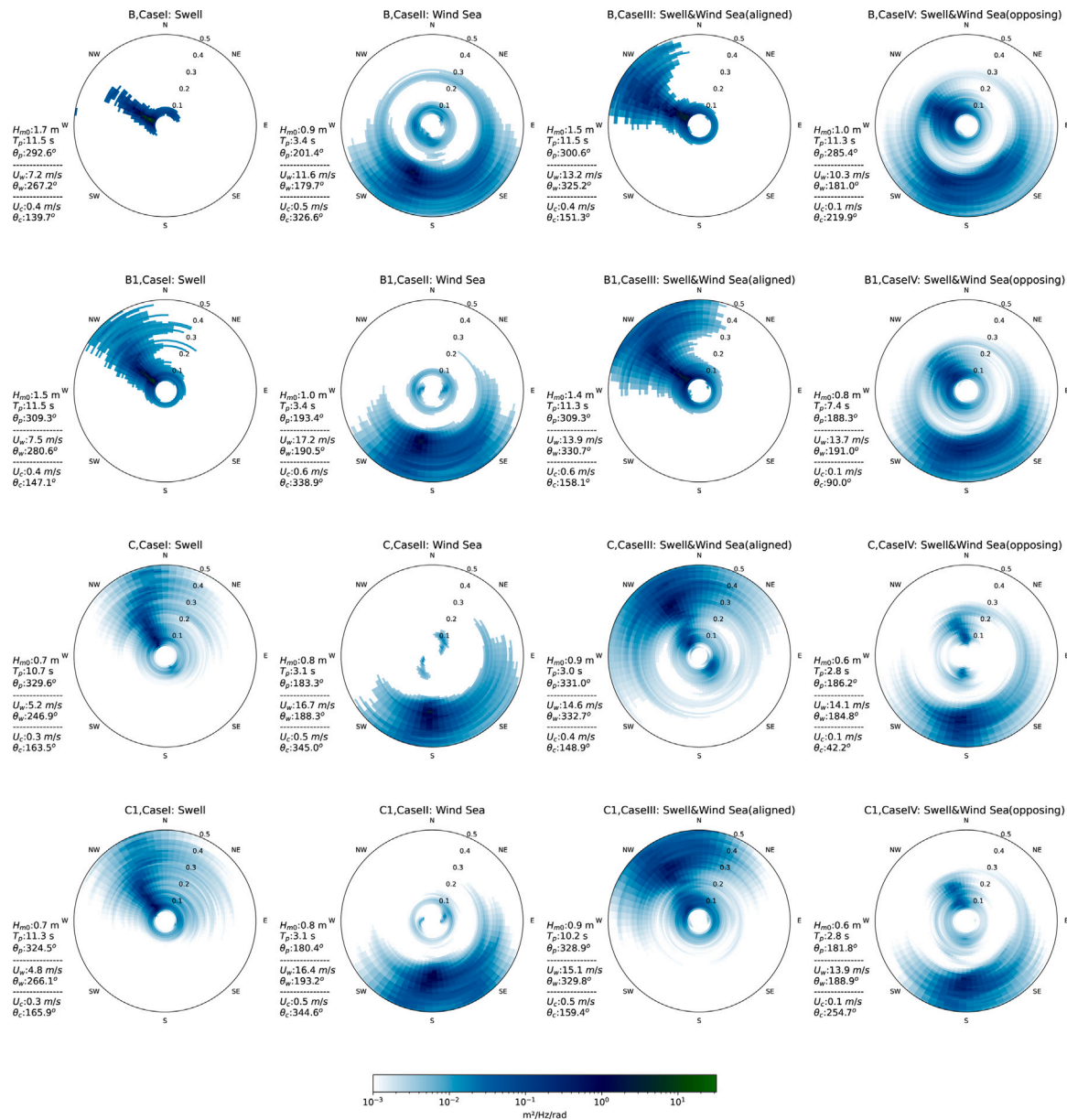
Fig. 10. Directional spectral density $S(f, \theta)$ at locations B, B1, C and C1 for the Cases I–IV (Table 1). The parameters H_{m0}, T_p, θ_p, U_w, θ_w, U_c and θ_c measured on the buoys indicate significant wave height (from spectrum), peak wave period, peak wave direction (meteorological convection), wind speed, wind direction (meteorological convection), surface current speed and surface current direction (oceanographic convection), respectively.

4. Discussion

Our overall results illustrate that the wave field is inhomogeneous across the fjord but nearly homogeneous along the fjord axis. Therefore, potential marine structures designed along the fjord axis, such as fish farms, floating solar panels and wave converters, will experience nearly homogeneous conditions. On the other hand, fjord-crossing infrastructures such as floating bridges will encounter inhomogeneous conditions that should be considered in the design.

In addition, we observe changes in wind sea energy between all locations. Even if the locations are relatively close to each other, there are differences in fetch geometry, which influences the wave growth. For example, when the wind blows from the south (cases II and IV), we observe differences in the wind sea part of the spectrum between locations B & C and B1 & C1 that affect the homogeneity. Nevertheless, these differences are relatively weak compared to the inhomogeneities during swell conditions due to sheltering effects induced by the fjord geometry.

The effect of surface currents on the wave field in Sulafjorden is weak (Christakos et al., 2021a). However, there are areas along the Norwegian coast, e.g. in Northern Norway where strong wave height modulations due to tidal currents have been found (Halsne et al., 2022). In such areas, we expect that surface currents may induce strong wave inhomogeneities.

The four measurement locations used in this study provide important information on the overall wave homogeneity and coherence in the fjord. Nevertheless, more measurements at a closer distance are needed to extract more concrete conclusions, e.g., by deploying additional wave buoys. For a floating bridge concept, the minimum distance between platoons can be 100–200 m. Thus, observations of wave characteristics at such distances need to be performed. However, the deployment distance between two buoys in deep water cannot be less than some hundreds of meters due to the long moorings and potential conflict with each other, which limits their applicability. Therefore, instruments that can measure spatio-temporal wave characteristics over a large ocean surface such as marine (X-band) radars (e.g., Dankert and
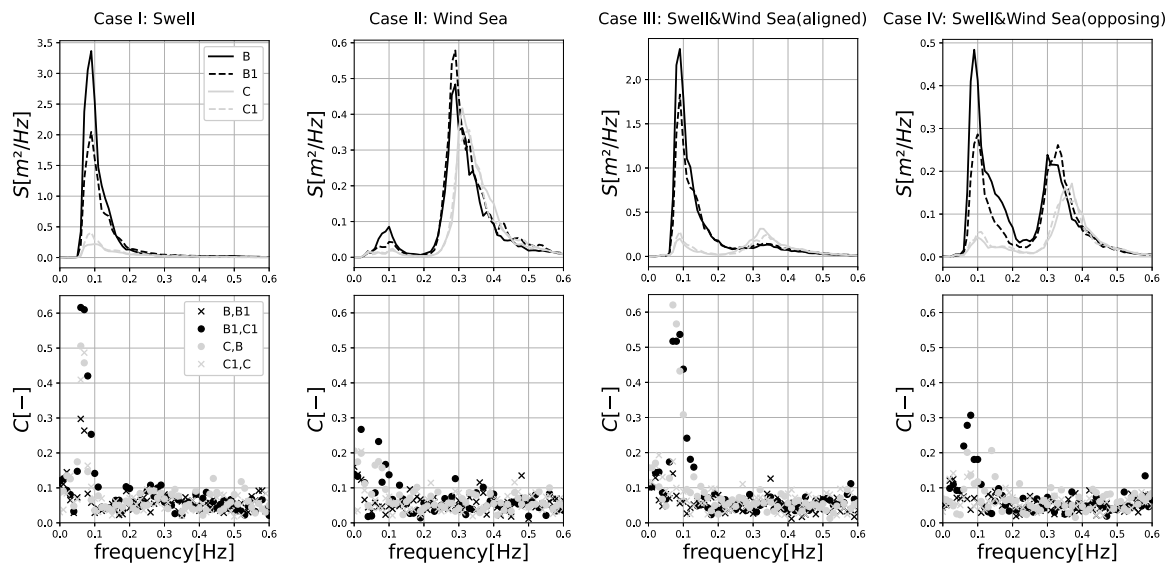
Fig. 11. Spectral densities (top) at B, B1, C and C1 buoys and coherence (bottom) between pairs during Cases I–IV (Table 1).
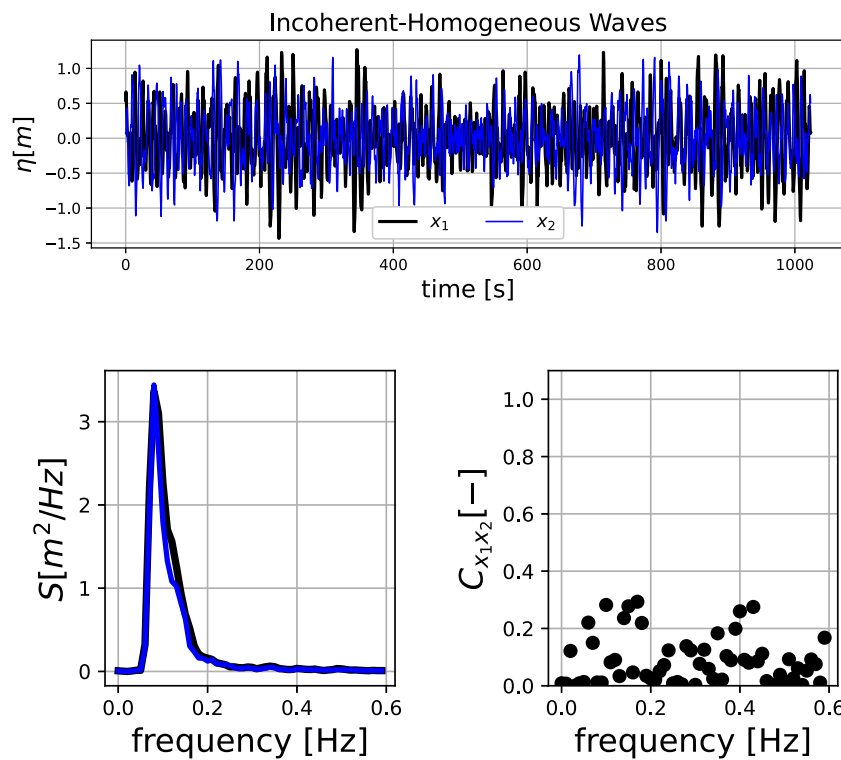

Fig. A.12. Example of surface elevation (η), spectral density (S) and coherence (C) for locations x_1 and x_2 during incoherent-homogeneous conditions ($C_{x_1 x_2} \ll 1$, $S_{x_1} - S_{x_2} \approx 0$).

Rosenthal, 2004; Huang et al., 2017; Nieto Borge et al., 2006, 2008; Young et al., 1985) and stereo-wave cameras (e.g., Benetazzo et al., 2012; Bergamasco et al., 2017; Fedele et al., 2013; Guimarães et al., 2020; Vieira et al., 2020) are more suitable for studying wave homogeneity and coherence at these scales. Smit et al. (2016) used a combination of X-band radar observations and the coupled-mode spectral analysis to identify coherent interference contributions in nearshore wave statistics. These advanced wave measurements can also be applied to establish a wave coherence model continuous in space. Then, the model can be used to generate random wave fields in numerical simulations, which are required to properly estimate the wave loads on large floating structures.

Numerical simulations can recreate the fjord wave conditions and provide a much denser spatial data grid than point observations. Phase-average models, such as SWAN (Booij et al., 1999) and STWAVE (Massey et al., 2011), are based on the radiative transfer equation (RTE), which describes the evolution of the variance density spectrum. Spectral models have successfully simulated coastal and fjord waves (e.g., Stefanakos et al., 2020; Christakos et al., 2020a, 2021a,b; Nygaard and Eik, 2004), but are not applicable for investigating wave coherence, since they simulate wave conditions stochastically via the spectrum. Phase-resolving models, again, simulate the actual surface elevation, and can be used to investigate wave homogeneity and coherence in coastal areas. Examples of such models are the fully nonlinear potential flow model, REEF3D::FNPF (Bihs et al., 2020; Wang et al.,
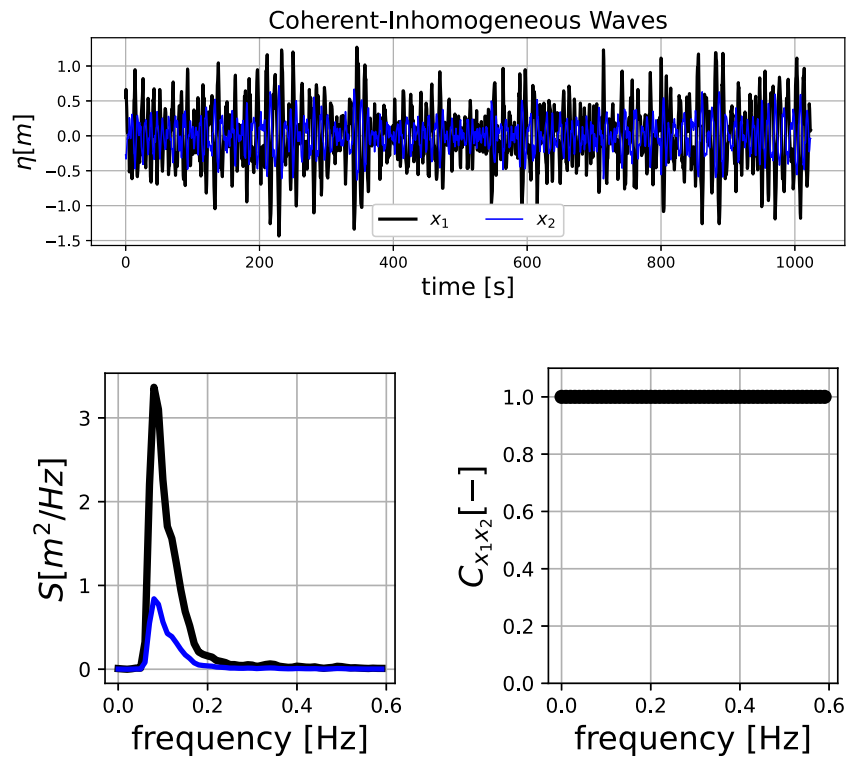
Fig. A.13. Example of surface elevation (η), spectral density (S) and coherence (C) for locations x_1 and x_2 during coherent-inhomogeneous conditions ($C_{x_1 x_2} = 1$, $|S_{x_1} - S_{x_2}| \gg 0$).
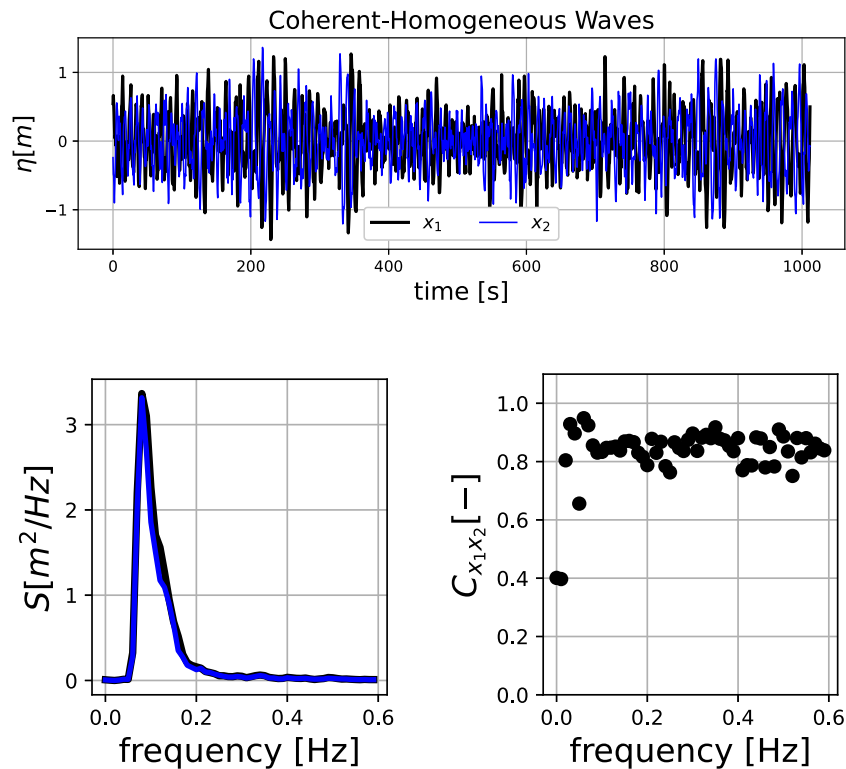

Fig. A.14. Example of surface elevation (η), spectral density (S) and coherence (C) for locations x_1 and x_2 during coherent-homogeneous conditions ($C_{x_1 x_2} \approx 1$, $S_{x_1} - S_{x_2} \approx 0$).

2022), and the non-hydrostatic shallow water model, SWASH, (Zijlema et al., 2011). For idealized cases with an arbitrary constant depth, a high order spectral model, such as the HOS-ocean model (Ducrozet et al., 2016), could also be applied to investigate wave homogeneity

and coherence due to nonlinear effects. However, to define the state of wave homogeneity and coherence based on numerical simulations, accurate wave spectrum and phase information are essential at the boundaries, e.g., using time series of observed surface elevation. In
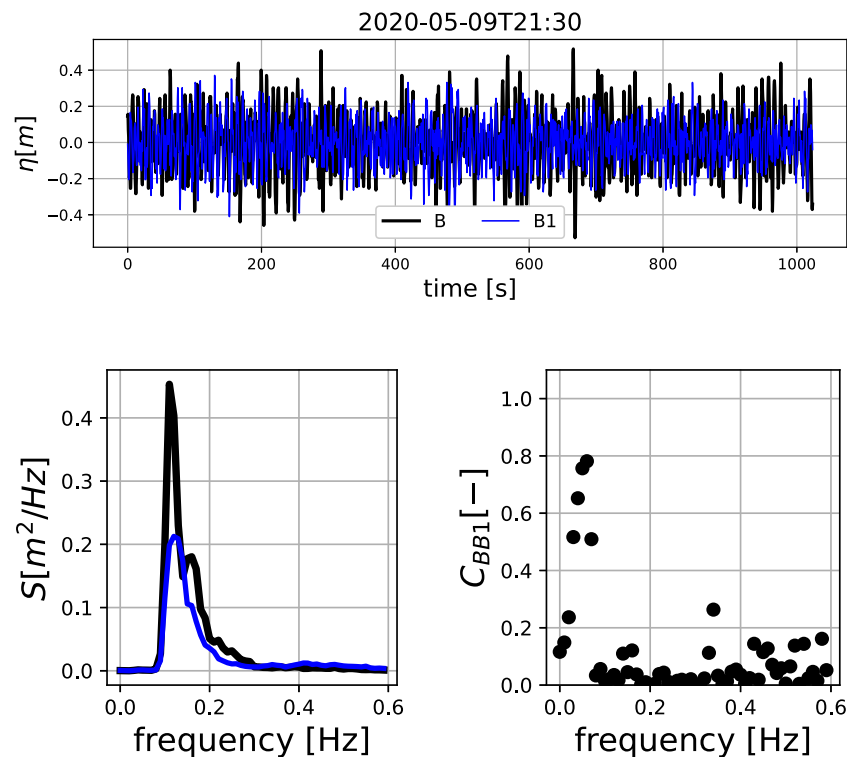
Fig. A.15. Surface elevation (η), spectral density (S) and coherence (C) for locations B and B1 at 2020-05-09T21:30.

addition, modeling of short-crested waves, e.g., local wind sea, in fjords is challenging for phase-resolving models due to the absence of a wind generation mechanism and the high spatial resolution grid that is required.

Based on ideas developed originally in optics, Smit and Janssen (2013) derived a generalization of the RTE for ocean waves based on a quasi-coherent (QC) approximation. The transported variable is a coupled-mode spectrum instead of the variance density spectrum. The coupled mode spectrum includes the effects of coherent interference via the evolution of cross-phase information. Smit et al. (2015) showed that the QC model simulates accurately nearshore crossing wave patterns which were neglected by the traditional phase-average models. Therefore, this stochastic model might prove useful for investigating coherent wave interference patterns also in fjords.

The results of this study can be applied to similar nearshore areas with fjords exposed to swell waves, e.g., in the Faroe Islands, Iceland, Greenland, Alaska, Chile, and New Zealand. Furthermore, our results can be valuable for numerical studies, providing insight into models' accuracy in reproducing the observed homogeneity and coherence levels.

5. Summary and conclusions

Offshore waves mostly dominate the wave climate in the Sulafjorden, a fjord partly exposed to the open ocean. The most exposed locations to the open sea (B & B1) are dominated by swell waves. However, in the most sheltered locations (C & C1), shorter waves (wind-sea) have often a spectral density comparable to swell.

Our results show that the wave field is inhomogeneous across the fjord axis but nearly homogeneous along the fjord. For locations across the fjord axis (B & C and B1 & C1), the wave conditions are inhomogeneous since their spectral density shows significant differences due to sheltering effects induced by the fjord geometry. However, for locations along the fjord axis (B & B1 and C & C1), the spectral density shows minor differences due to direct exposure to the same wave energy trajectory coming from the open ocean (e.g., swell), resulting

in homogeneous conditions. These locations experience the same swell wave with a time lag, often exhibiting a low coherence (randomly distributed phases).

On the other hand, for locations across the fjord axis (B & C and B1 & C1), the penetration of swell in the fjord is linked to high coherence. Due to the long crests of swell-type waves, the pairs across the fjord axis frequently experience the motion of the same individual wave. Therefore, these locations often encounter a constant phase difference (or a lower degree of randomness in phase difference), revealing high coherence values.

The wind sea has low coherence along and across the fjord axis and in all wind and wave conditions. The wind sea in the fjord system has crest lengths typically much smaller than buoy distances (0.6–2 km), leading to a high degree of phase-randomness and low coherence. Furthermore, during wind sea conditions, the wave elevations at two locations are the summation of short-crested wave components generated from different directions/fetches, resulting in low coherence.

As expected, there is no direct link between wave coherence and homogeneity. Based on our observations, the highest coherence values between the different pairs are associated with frequencies close to the spectral peak, where the highest difference in spectral density (inhomogeneity) is observed.

CRediT authorship contribution statement

Konstantinos Christakos: Conceptualization, Methodology, Software, Formal analysis, Investigation, Data curation, Writing – original draft, Writing – review & editing, Visualization. **Zhen Gao:** Methodology, Supervision, Writing – review & editing, Project administration. **Birgitte R. Furevik:** Methodology, Writing – review & editing. **Jan-Victor Björkqvist:** Methodology, Writing – review & editing. **Ole Johan Aarnes:** Writing – review & editing.

Declaration of competing interest

The authors declare that they have no known competing financial interests or personal relationships that could have appeared to influence the work reported in this paper.

Data availability

Acknowledgments

Appendix

See Figs. A.12–A.15.

References

Aalberg, A., 2017. Analysis and Design Bjørnefjorden Floating Cable-Stayed Bridge subjected to Large Ship Collisions and Extreme Environmental Loads (Master thesis). NTNU, Trondheim, Norway, NTNU, Norwegian University of Science and Technology, Trondheim.

Aksnes, V., Alsos, H., Bachynski, E., et al., 2022. On common research needs for the next generation of floating support structures. In: Proceedings of the ASME 2022 41st International Conference on Ocean, Offshore and Arctic Engineering OMAE2022. OMAE.

Ananth, P.N., Tatavarti, R.V., Swain, J., Rao, C.V., 1993. Observations of sea and swell using directional wave buoy. Proc. Indian Acad. Sci.-Earth Planet. Sci. 102 (2), 351–366.

Bendat, J., Piersol, A., 2010. Random Data: Analysis and Measurement Procedures, fourth ed. Wiley.

Benetazzo, A., Fedele, F., Gallego, G., Shih, P.-C., Yezzi, A., 2012. Offshore stereo measurements of gravity waves. Coast. Eng. 64.

Bergamasco, F., Torsello, A., Sclavo, M., Barbariol, F., Benetazzo, A., 2017. WASS: An open-source pipeline for 3D stereo reconstruction of ocean waves. Comput. Geosci. 107.

Bihs, H., Wang, W., Pakozdi, C., Kamath, A., 2020. REEF3D::FNPF—A flexible fully nonlinear potential flow solver. J. Offshore Mech. Arct. Eng. 142 (4).

Booij, N., Ris, R.C., Holthuijsen, L.H., 1999. A third-generation wave model for coastal regions: 1. Model description and validation. J. Geophys. Res.: Oceans 104 (C4), 7649–7666.

Brissette, F.P., Tsanis, I.K., 1994. Estimation of wave directional spectra from pitch-roll buoy data. J. Waterw. Port Coast. Ocean Eng. 120 (1), 93–115.

Cheng, Z., Svangstu, E., Moan, T., Gao, Z., 2021. Assessment of inhomogeneity in environmental conditions in a Norwegian Fjord for design of floating bridges. Ocean Eng. 220.

Christakos, K., 2021. Ferjefri-E39_MET-Norway (Metocean analysis tools for Ferjefri E39 dataset). GitHub Repository, URL https://github.com/KonstantinChri/Ferjefri-E39_MET-Norway.git.

Christakos, K., Björkqvist, J.V., Breivik, Ø., Tuomi, L., Furevik, B.R., Albretsen, J., 2021a. The impact of surface currents on the wave climate in narrow Fjords. Ocean Model. 168, 101894, URL https://www.sciencedirect.com/science/article/pii/S1463500321001475.

Christakos, K., Björkqvist, J.-V., Tuomi, L., Furevik, B.R., Breivik, Ø., 2021b. Modelling wave growth in narrow fetch geometries: The white-capping and wind input formulations. Ocean Model. 101730.

Christakos, K., Furevik, B.R., Aarnes, O.J., Breivik, Ø., Tuomi, L., Byrkjedal, Ø., 2020a. The importance of wind forcing in Fjord wave modelling. Ocean Dyn. 70 (1), 57–75.

Christakos, K., Reuder, J., Furevik, B., 2013. Experimental characterization of the Marine atmospheric boundary layer in the Havsul area, Norway. Energy Procedia 35, 121–127.

Christakos, K., Varlas, G., Cheliotis, I., Spyrou, C., Aarnes, O.J., Furevik, B.R., 2020b. Characterization of wind-sea- and swell-induced wave energy along the Norwegian Coast. Atmosphere 11 (2), URL https://www.mdpi.com/2073-4433/11/2/166.

Christakos, K., Varlas, G., Reuder, J., Katsafados, P., Papadopoulos, A., 2014. Analysis of a low-level coastal jet off the Western Coast of Norway. Energy Procedia 53, 162–172.

Dai, J., Leira, B.J., Moan, T., Alsos, H.S., 2021a. Effect of wave inhomogeneity on fatigue damage of mooring lines of a side-anchored floating bridge. Ocean Eng. 219.

Dai, J., Stefanakos, C., Leira, B.J., Alsos, H.S., 2021b. Effect of modelling inhomogeneous wave conditions on structural responses of a very long floating bridge. J. Mar. Sci. Eng. 9 (5).

Dankert, H., Rosenthal, W., 2004. Ocean surface determination from X-band radar-image sequences. J. Geophys. Res. 109, 1–11.

Donelan, M., Pierson, W.J., 1983. The sampling variability of estimates of spectra of wind-generated gravity waves. J. Geophys. Res. 88 (C7), 4381–4392.

Ducrozet, G., Bonnefoy, F., Le Touzé, D., Ferrant, P., 2016. HOS-ocean: Open-source solver for nonlinear waves in open ocean based on High-Order Spectral method. Comput. Phys. Comm. 203, 245–254.

Dunham, K.K., 2016. Coastal highway route E39 - Extreme crossings. Transp. Res. Proc. 14, 494–498.

Fedele, F., Benetazzo, A., Gallego, G., Shih, P.C., Yezzi, A., Barbariol, F., Ardhuin, F., 2013. Space–time measurements of oceanic sea state. Ocean Model. 70, 103–115.

Forristall, G.Z., Heideman, J.C., Leggett, I.M., Roskam, B., Vanderschuren, L., 1996. Effect of sampling variability on hindcast and measured wave heights. J. Waterw. Port Coast. Ocean Eng. 122 (5), 216–225.

FUGRO, 2012. SEAWATCH wavescan buoy. URL https://www.fugro.com/docs/default-source/about-fugro-doc/ROVs/seawatch-wavescan-buoy-flyer.pdf.

Furevik, B.R., Lønseth, L., Borg, A.L., Neshaug, V., Gausen, M., 2020. Oceanographic Observations for the Coastal Highway E39 Project in Mid-Norway. The Norwegian Meteorological Institute, URL https://thredds.met.no/thredds/catalog/obs/mast-svv-e39/catalog.html.

Guimarães, P.V., Ardhuin, F., Bergamasco, F., Leckler, F., Filipot, J.F., Shim, J.S., Dulov, V., Benetazzo, A., 2020. A data set of sea surface stereo images to resolve space-time wave fields. Sci. Data 7 (1).

Halsne, T., Bohlinger, P., Christensen, K.H., Carrasco, A., Breivik, Ø., 2022. Resolving regions known for intense wave–Current interaction using spectral wave models: A case study in the energetic flow fields of Northern Norway. Ocean Model. 176.

Hasselmann, S., Brüning, C., Hasselmann, K., Heimbach, P., 1996. An improved algorithm for the retrieval of ocean wave spectra from synthetic aperture radar image spectra. J. Geophys. Res. C: Oceans 101 (C7), 16615–16629.

Huang, W., Liu, X., Gill, E.W., 2017. Ocean wind and wave measurements using X-band marine radar: A comprehensive review. Remote Sens. 9 (12).

International Eletrotechnical Commision, 2005. IEC 61400-1 Wind Turbines - Part 1: Design requirements. In: Wind Turbines – Part 1: Design Requirements, Vol. 2005.

Komen, G.J., Hasselmann, S., Hasselmann, K., 1984. On the existence of a fully developed wind-sea spectrum. J. Phys. Oceanogr. 14 (8), 1271–1285.

Longuet-Higgins, M.S., 1963. The effect of non-linearities on statistical distributions in the theory of sea waves. J. Fluid Mech. 17 (3), 459–480.

Lygre, A., Krogstad, H.E., 1986. Maximum entropy estimation of the directional distribution in ocean wave spectra. J. Phys. Oceanogr. 16 (12), 2052–2060, URL https://journals.ametsoc.org/view/journals/phoc/16/12/1520-0485_1986_016_2052_meeotd_2_0_co_2.xml.

Mandel, L., Wolf, E., 1995. Optical Coherence and Quantum Optics. Cambridge University Press, URL https://www.cambridge.org/core/product/identifier/9781139644105/type/book.

Mann, J., 1994. The spatial structure of neutral atmospheric surface-layer turbulence. J. Fluid Mech. 273.

Massey, T.C., Anderson, M.E., Smith, J.M., Gomez, J., Jones, R., 2011. STWAVE: Steady-State Spectral Wave Model User's Manual for STWAVE, Version 6.0. Tech. Rep., US Army Corps of Engineers.

Nieto Borge, J.C., Hessner, K., Jarabo-Amores, M.-P., de la Mata-Moya, D., 2008. Signal-to-noise ratio analysis to estimate ocean wave heights from X-band marine radar image time series. Radar Sonar Navig. IET 2, 35–41.

Nieto Borge, J.C., Jarabo-Amores, P., De La Mata-Moya, D., López-Ferreras, F., 2006. Estimation of ocean wave heights from temporal sequences of X-band marine radar images. In: European Signal Processing Conference.

Nygaard, E., Eik, K.J., 2004. Application of STWAVE in Norwegian Coastal waters. In: 8th International Workshop on Wave Hindcasting & Forecasting. North Shore, Oahu, Hawaii.

Radoski, H.R., Fougere, P.F., Zawalick, E.J., 1975. A comparison of power spectral estimates and applications of the maximum entropy method. J. Geophys. Res. 80 (4), 619–625.

Salatin, R., Chen, Q., Bak, A.S., Shi, F., Brandt, S.R., 2021. Effects of wave coherence on longshore variability of nearshore wave processes. J. Geophys. Res.: Oceans 126 (11).

Semedo, A., Vettor, R., Breivik, Ø., Sterl, A., Reistad, M., Lima, D., 2014. The wind sea and swell waves climate in the Nordic seas. Ocean Dyn. 65.

Sjødivisjon, K., 2015. Produktark: Sjøterrengmodeller. Tech. Rep., Kartverket (Norwegian Mapping and Cadastre Authority), URL http://wms.geonorge.no/skwms1/wms.havbunnrast.

Smit, P.B., Bland, R., Janssen, T.T., Laughlin, B., 2016. Remote sensing of nearshore wave interference. J. Geophys. Res.: Oceans 121 (5), 3409–3421.

Smit, P.B., Janssen, T.T., 2013. The evolution of inhomogeneous wave statistics through a variable medium. J. Phys. Oceanogr. 43 (8), 1741–1758.

Smit, P.B., Janssen, T.T., Herbers, T.H., 2015. Stochastic modeling of coherent wave fields over variable depth. J. Phys. Oceanogr. 45 (4), 1139–1154.

Steele, K.E., Wang, D.W., Earle, M.D., Michelena, E.D., Dagnall, R.J., 1998. Buoy pitch and roll computed using three angular rate sensors. Coast. Eng. 35 (1–2), 123–139.

Stefanakos, C., Furevik, B.R., Knutsen, Ø., Christakos, K., 2020. Nearshore wave modelling in a Norwegian Fjord. In: Proceedings of the ASME 2020 39th International Conference on Ocean, Offshore and Arctic Engineering, Vol. 6B:Ocean E.

Stoica, P., Moses, R., 2005. Spectral Analysis of Signals. Prentice Hall.

The Norwegian Ministry of Transport, 2020. Meld. St. 20 (2020–2021) Report to the Storting (White Paper). National Transport Plan 2022–2033. Tech. Rep., The Norwegian Ministry of Transport.

Vieira, M., Guimarães, P.V., Violante-Carvalho, N., Benetazzo, A., Bergamasco, F., Pereira, H., 2020. A low-cost stereo video system for measuring directional wind waves. J. Mar. Sci. Eng. 8 (11).

Wang, W., Pakozdi, C., Kamath, A., Fouques, S., Bihs, H., 2022. A flexible fully nonlinear potential flow model for wave propagation over the complex topography of the Norwegian Coast. Appl. Ocean Res. 122 (February).

Welch, P., 1967. The use of fast Fourier transform for the estimation of power spectra: A method based on time averaging over short, modified periodograms. IEEE Trans. Audio Electroacoust. 15, 70–73.

Young, I.R., Rosenthal, W., Ziemer, F., 1985. A three-dimensional analysis of marine radar images for the determination of ocean wave directionality and surface currents. J. Geophys. Res. 90 (C1).

Zijlema, M., Stelling, G., Smit, P., 2011. SWASH: An operational public domain code for simulating wave fields and rapidly varied flows in coastal waters. Coast. Eng. 58 (10), 992–1012.